

Deep Learning-Based Reconstruction of Interventional Tools from Four X-Ray Projections for Tomographic Interventional Guidance

Elias Eulig, Joscha Maier, Michael Knaup, N. Robert Bennett, Klaus Hörndler, Adam S. Wang, and Marc Kachelrieß

Abstract—Image guidance for minimally invasive interventions is usually performed by acquiring fluoroscopic images using a C-arm system. However, the projective data provide only limited information about the spatial structure and position of interventional tools such as stents, guide wires or coils. In this work we propose a deep learning-based pipeline for real-time tomographic (four-dimensional) interventional guidance at acceptable dose levels. In the first step, interventional tools are extracted from four cone-beam CT projections using a deep convolutional neural network (CNN). These projections are then reconstructed and fed into a second CNN, which maps this highly undersampled reconstruction to a segmentation of the interventional tools. Our pipeline is capable of reconstructing interventional tools from only four x-ray projections without the need for a patient prior with very high accuracy. Therefore, the proposed approach is capable of overcoming the drawbacks of today's interventional guidance and could enable the development of new minimally invasive radiological interventions by providing full spatiotemporal information about the interventional tools.

Index Terms—Computed tomography, cone-beam CT, convolutional neural network, image-guided surgery, interventional radiology, medical imaging, minimally invasive.

I. INTRODUCTION

IN the past decades minimally invasive interventions replaced conventional surgery in many areas and enabled the development of new diagnostic and therapeutic procedures including angiography [1]–[4], biopsy [5], angioplasty using

stents [6], and embolization using coils or other emboli [7]–[11]. These interventions demand precise image guidance, commonly accomplished by single- or biplane x-ray fluoroscopy with typical frame rates ranging between 7.5 and 15 frames per second [12]. Such (projective) acquisitions may be supported with 3D information by occasionally acquiring cone-beam CT (CBCT) scans during the intervention [13]. However, fluoroscopy as the main source of guidance is drastically limited in its ability to resolve the three-dimensional structures and locations of the interventional material, potentially hindering the development of new procedures [14].

Tomographic (four-dimensional) image guidance would be capable of overcoming this drawback by providing full spatiotemporal information about the interventional tools. However, to be conducted at comparable update rates as fluoroscopic image guidance and using fully sampled datasets with conventional reconstruction algorithms, would result in excessively high radiation dose to both the patient and the surgeon [15]. Prior work has shown that it is possible to reconstruct interventional tools from 16 projections (without allowing for temporal overlap) using the principles of compressed sensing theory [16], [17]. The PrIDICT algorithm [18], [19] assumes that the rawdata difference between a forward-projected patient prior (a fully sampled patient scan acquired prior to the intervention) and the interventional data acquired at time step t is zero everywhere (up to noise), except for those detector pixels, where interventional tools are present. The reconstructed volume is deteriorated in image quality due to streak artifacts coming from the high angular under-sampling. To solve this problem the authors further assume that the interventional tools are of high contrast, therefore the insignificant voxels can be set to zero through a thresholding operation and the resulting volume is sparse, containing only the interventional tools. Adding this volume to the patient prior yields the result of the PrIDICT algorithm

$$f_t^{\text{PrIDICT}} = f_p + \theta \left(X^{-1} (p_t - X f_p) \right), \quad (1)$$

where f_p denotes the patient prior, p_t the rawdata acquired during the intervention, X the forward projection operator, X^{-1} the Feldkamp-David-Kress (FDK) [20] reconstruction, and θ the thresholding operator. Since the first assumption holds only in the absence of patient motion, it is necessary to register the patient prior before subtracting it from the interventional data.

Parts of the reconstruction and simulation software were provided by RayConStruct® GmbH, Nürnberg, Germany. This work was supported in part by the Society of High Performance Computational Imaging (SHPCI) e.V., Nürnberg, Germany and the National Center for Research Resources of the National Institutes of Health under award number S10RR026714. Some of the computing for this project was performed on the Sherlock cluster. We would like to thank Stanford University and the Stanford Research Computing Center for providing computational resources and support that contributed to these research results.

Elias Eulig is with the Department of X-Ray Imaging and Computed Tomography, German Cancer Research Center (DKFZ), Heidelberg, Germany and also with the Department of Radiology, Stanford University, Stanford, USA. E-mail: elias.eulig@dkfz.de.

Dr. Joscha Maier, Dr. Michael Knaup, and Prof. Dr. Marc Kachelrieß are with the Department of X-Ray Imaging and Computed Tomography, German Cancer Research Center (DKFZ), Heidelberg, Germany.

N. Robert Bennett and Dr. Adam S. Wang are with the Department of Radiology, Stanford University, Stanford, USA.

Klaus Hörndler is with Ziehm Imaging GmbH, Nürnberg, Germany.

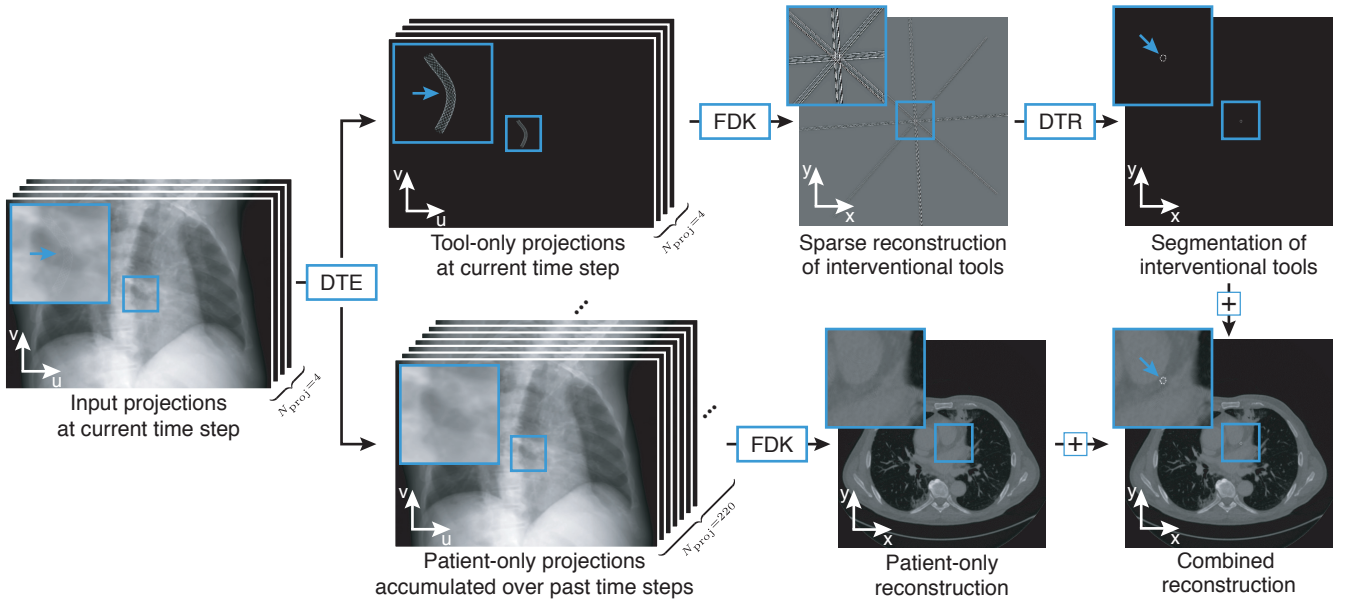


Fig. 1. Illustration of a deep learning-based tomographic interventional guidance. Projections are acquired continuously in which the DTE separates interventional tools from the patient background. While the reconstruction of interventional tools (upper path) is fully updated with every new set of four projections, the patient volume is reconstructed with temporal overlap using a sufficient amount of projections from distinct angles (lower path). The two volumes can be added to yield the final reconstruction.

Here, a deformable volume-to-rawdata (3D-2D) registration method is preferred over a volume-to-volume (3D-3D) one in order to exclude the influence of undersampling artifacts in the image domain from the registration process [21].

However, the resulting pipeline of deformable volume-to-rawdata (3D-2D) registration method and PrIDICT algorithm as proposed in [21] has two main disadvantages. Firstly, the radiation dose levels are still approximately a factor 16 higher than those present in today's single- or biplane fluoroscopy. Secondly, the 3D-2D registration method is too computationally intensive to realize the pipeline in real-time, which would be a requirement for clinical practice.

Recently, to overcome the dose accumulation problem, we proposed the deep tool reconstruction (DTR) [22], [23], which is capable of reconstructing stents and guide wires from only four x-ray projections. Given that a patient prior is perfectly registered, this is achieved by training a CNN to learn a mapping from the corresponding sparse view CT reconstruction to a segmentation of the interventional tools.

In this work, we improve this method further by firstly, letting the network consider the three-dimensional context of the interventional tools rather than just two-dimensional slices and thereby improving its accuracy significantly. Secondly, we train the network jointly on guide wires, stents and coils, and thirdly, test it on scans of commercially available stents, guide wires and coils.

Furthermore, to eliminate the need for a prior volume and a computationally intensive registration step we introduce another CNN (referred to as deep tool extraction, DTE) in the projection domain, where interventional tools can be easily located and extracted from the background. Additionally, this eliminates the need for a patient prior, thus easing the clinical workflow and reducing the patient dose further.

II. MATERIAL AND METHODS

A novel, deep learning-based pipeline is developed, which can reconstruct the interventional tools during a procedure from only four x-ray projections and without the need for a prior scan. The method is comprised of two networks, $DTE(\cdot; \epsilon)$ and $DTR(\cdot; \rho)$, where ϵ, ρ denote their respective set of parameters. Firstly, the DTE network extracts the interventional tools in projections p_t . These projections are then FDK reconstructed, yielding a volume with severe streak artifacts in the reconstruction that arise due to the heavy undersampling. We leverage FDK as a known operator to reconstruct using the known system geometry, as opposed to trying to learn this transform. Then, the DTR network is applied in image domain to segment the interventional tools present in the reconstruction. During an intervention the segmentation would be added onto a continuously updated patient volume f_p , yielding the final volume

$$f_t = f_p + DTR(X^{-1}DTE(p_t; \epsilon); \rho) \quad (2)$$

A. System Specification

We assume a gantry comprised of four x-ray tubes and flat detectors respectively, arranged with an angular spacing of 45° . While the gantry rotates, new sets of projections are acquired continuously, s.t. the reconstruction of interventional tools (upper path in Fig. 1) can be updated with every new set of four projections. The patient volume (lower path in Fig. 1) can be FDK-reconstructed with a temporal overlap using the patient-only projections accumulated over several past time steps. While such a system is yet to be developed, the methodology presented here is not restricted to this particular design and alterations involving fewer x-ray tubes and flat detectors potentially combined with temporally overlapping reconstructions may be made.

TABLE I
OVERVIEW OF SYSTEM SPECIFICATIONS OF THE ZEEGO
ROBOT-DRIVEN C-ARM SYSTEM USED IN THIS STUDY.

Specification	Description
Focal-spot-to-detector distance	1200 mm
Focal-spot-to-isocenter distance	785 mm
Detector size	40 cm × 30 cm
Detector material	a-Si with CsI(Tl) scintillator
Pixel size d_{uv}	308 μ m
Matrix size $N_u \times N_v$	1240 × 960
# of projections over π + fan angle	496
Field of measurement (FOM)	25 cm
Tube voltage	90 kV

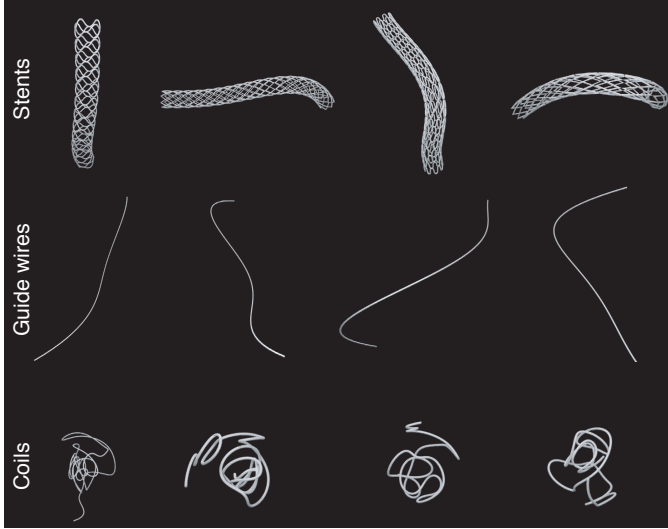


Fig. 2. Some examples for 3D models of stents, coils and guide wires used to train and validate both DTE and DTR.

For all simulations and measurements a Zeego robot-driven C-arm system (Siemens Healthineers, Forchheim, Germany) with specifications given in Table I is employed.

B. Simulations

1) *3D Models*: 3D models of guide wires, coils and stents are generated through the Python API of Blender [24] with randomly varying parameters within a range such that the models reflect a wide range of commercially available tools. The resulting models are then saved as triangular meshes (STL file format) for the CT data simulation. In total, the dataset comprises 600 3D models of guide wires, stents and coils (200 each), some of which are depicted in Fig. 2.

The guide wires are simulated as cylinders with varying diameter (randomly chosen in the range of 0.4 to 0.8 mm based on specifications of commercial guide wires) along a non-uniform rational basis-spline (NURBS) curve with five control points, evenly spaced along the z-axis. In order to deform the curve, between two and four points are randomly shifted in the x-y plane based on a multivariate normal distribution with $\mu = 0$ and $\sigma = 2.5$ cm. The resulting models are then randomly rotated along all three axes, to ensure that the training data are not biased towards a specific orientation of the guide wires.

Each stent model is based on one out of eight base models, with varying stent diameters and strut thicknesses. The diameters are randomly chosen in the range from 4.8 to 6.3 mm and

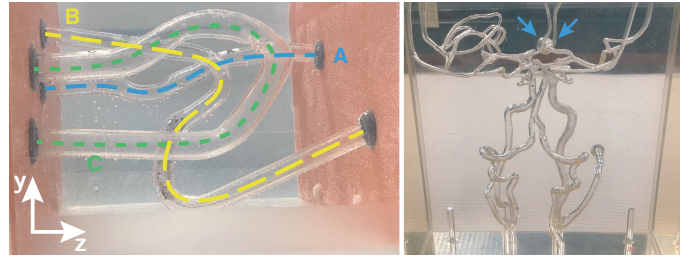


Fig. 3. Custom vessel phantom (left) and commercial brain-vessel phantom (right) with a saccular aneurysm (blue arrows). The scans acquired using these phantoms were used to test the proposed pipeline.

the strut thicknesses are randomly chosen in the range from 0.4 to 0.7 mm based on specifications of commercial stents. The resulting models are placed along a similar NURBS curve as the guide wires and between one and three of the control points are randomly shifted in the x-y plane based on a multivariate normal distribution with $\mu = 0$ and $\sigma = 1$ cm. Finally, the models are randomly rotated along each of the x, y, and z-axis.

The coil models are generated by placing between 30 and 60 control points within a sphere of a diameter between 10 mm and 30 mm. The control points are placed equidistantly from each other and with a minimum opening angle of 45° to prevent unrealistically strong kinks. Then, the sorted points are connected through a NURBS curve with each other. A cylinder with diameter between 0.4 and 0.8 mm following this curves yields the final 3D model.

2) *CT Data Simulation*: To simulate cone-beam projections, the simulated tools are randomly placed within the FOM of the scanner and polychromatically forward-projected according to the Zeego geometry. The material of the tools is simulated to be iron of varying density (between 3.2 and 3.9 g/cm³), such that the resulting absorption coefficients match the ones of commercially available tools. For the training of the DTE network 17 projections per 3D model were simulated with an angular spacing of 10° and the resulting projections were cropped around the interventional tools prior to loading them into the training pipeline described in Sec. II-D.

For the training of the deep tool reconstruction the models are forward projected from four projections with an angular spacing of 45° and a random start angle. The volume around the tools is reconstructed using a FDK reconstruction with an isotropic voxel size of $100 \mu\text{m}^3$. The respective voxel representations of the STL files serve as ground truth.

C. Measurements

Ideally, our method would be tested on CT scans from real interventions, together with a ground truth segmentation of the interventional tools. However, CBCTs are rarely being acquired during interventions and for these an acceptable segmentation is often not available. Hence, in order to obtain a good estimate of the potential performance on clinical data, the method is tested on phantom measurements instead.

To this end, scans of interventional tools, namely guide wires, stents and a coil are acquired using two different intervention phantoms. For the measurement of stents and guide

wires a vessel phantom (Fig. 3) is designed and constructed, consisting of artificial vessels in a water container, in which the stents and guide wires can be inserted. They are then scanned in a variety of different positions, leading to different deformations of the tools. For the measurements of the coil a commercial brain vessel phantom of the circle of Willis is used (Elastrat Sàrl, Geneva, Switzerland). The coil is inserted in a saccular aneurysm at the right A1 segment of the anterior cerebral artery (Fig. 3, blue arrows) and several scans are acquired at different insertion depths.

To obtain the ground truth, we acquired prior scans of the phantom only and subtracted the projections from the interventional ones for all 496 projections. Thresholding after the FDK reconstruction yields the desired ground truth segmentation.

D. Deep Tool Extraction (DTE)

In order to eliminate the need for both a patient prior and a computationally intensive registration algorithm as it was the case in [18], [19], [21], the interventional tools are extracted directly in the raw data domain using a CNN. From an arbitrary projection showing interventional tools in a patient, this network is trained to predict the projection values of the interventional tools only.

Note that conceptually, this is very similar to DeepDSA [25], [26], where a CNN is trained to extract vessels from contrast-enhanced x-ray fluoroscopy data.

1) *Data Preprocessing*: For training and validation of the network, simulated forward projections of interventional tools which are added onto projections of CBCT patient scans serve as input and the respective projections of interventional tools serve as ground truth. Projections from four CBCT patient scans (two thorax, one head and one pelvis) are used for training and the projections from two CBCT patient scans (one thorax and one abdomen) are used for validation. Training and validation is performed patch-wise on patches of size 384×384 pixels which are randomly cropped from random projections of the patient scans. To reduce the amount of training data with interventional tools placed outside the patient we reject those patches with no or minor attenuation. The projections of the tools are then randomly flipped in x-y direction to cover the remaining 180° , which were not simulated and are added to the patient patch in a random position.

To let the network generalize to different noise levels, we simulate quantum noise using a Poisson distribution for varying tube currents. Furthermore, to let the network generalize to different point spread functions (PSFs), angular blurring from the rotation of the scanner, and small movements of the interventional tools, the projections are blurred with a multivariate Gaussian kernel with standard deviations sampled uniformly between 0 and 1.4 pixels.

Since all data preprocessing is performed in an online manner, we estimate the mean and standard deviation of projection values using a running mean μ and running variance σ^2 [27], [28]. Each sample is then normalized with the current μ s and σ s, such that the training data are normalized to zero mean and unit variance at any time.

2) *Training Details*: As network $DTE_{\bar{\epsilon}}$, we use a standard U-Net [29] comprised of four stages in both the encoding path and the decoding path. Here, each stage is composed of two convolutional layers (kernel size = 3×3 , stride = 1×1 , zero padding) each followed by a batch normalization layer [30], a spatial dropout layer [31] with dropout probability 0.2 to reduce overfitting and a rectified linear unit (ReLU) [32]. The encoding path performs a progressive spatial downsampling by employing 2×2 max-pooling after each stage while increasing the feature dimension by a factor of two starting with 64 in the first layer. The upsampling in the decoding path is performed by a nearest-neighbor upsampling operation followed by a convolutional layer (kernel size = 3×3 , stride = 1×1 , zero padding). Concatenative skip connections between the encoding and the decoding path allow high-resolution information from the earlier layers to skip the bottleneck. All convolutional layers of the network are initialized using He initialization [33] while the weights of the batch normalization layers are initialized with unity and their biases with zeros.

The training pipeline is implemented using PyTorch [34]. The optimal parameters $\hat{\epsilon}$ are determined by minimizing the \mathcal{L}_1 loss between network output $DTE(x; \epsilon)^{(n)}$ and ground truth $y^{(n)}$ on mini-batches of size $N = 6$

$$\hat{\epsilon} = \arg \min_{\epsilon} \frac{1}{N \times K^2} \sum_{n,k} \|DTE(x; \epsilon)_k^{(n)} - y_k^{(n)}\|_1, \quad (3)$$

where the sum runs over all samples $0 \leq n < N$ and pixels $0 \leq k < K^2$, respectively. To this end, the Adam optimizer [35] with a learning rate $\alpha = 1 \times 10^{-4}$ and parameters $\beta_1 = 0.9$, $\beta_2 = 0.999$ is employed.

E. Deep Tool Reconstruction (DTR)

The second stage of our pipeline takes as input several sparse FDK reconstructions of tool-only projections that are obtained by the DTE. By doing so, DTR is able to learn 3D features about the structure of the interventional tools. The deep tool reconstruction is then trained to predict the segmentation of the corresponding interventional tools.

1) *Data Preprocessing*: During training the network takes as input chunks of C patches of size 224×224 pixels, with C as an uneven number of reconstructed slices. These chunks are randomly cropped from the FDK reconstruction together with the ground truth of the center slice. Prior to feeding the reconstructions to the network they are normalized to have zero mean and unit variance.

2) *Training Details*: The DTR network is very similar to the DTE network, with two differences. Firstly, the multi-channel input to the network are the aforementioned C x-y slices of the sparse FDK reconstruction. Secondly, for the final layer of the DTR network we employ a sigmoid, rather than a ReLU as nonlinearity.

The training pipeline is implemented using PyTorch [34]. Training is performed with a mini-batch size of $N = 16$ and we employ Adam [35] ($\alpha = 1 \times 10^{-4}$, $\beta_1 = 0.9$, $\beta_2 = 0.999$) to minimize the soft Dice loss with Laplace smoothing between the ground truth segmentation of the center slice $y^{(n)}$

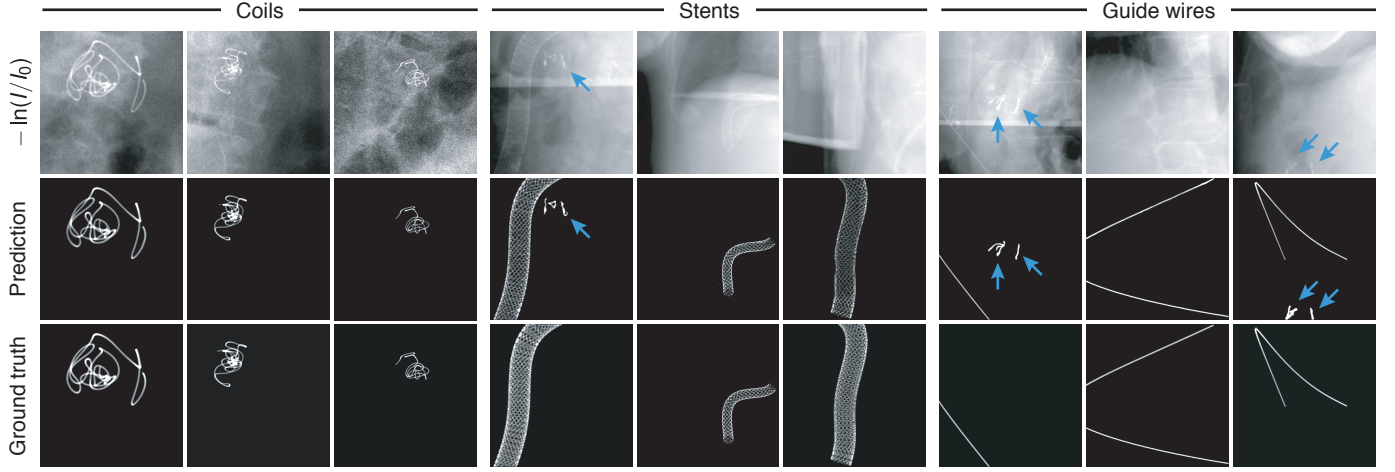


Fig. 4. Application of the deep tool extraction to nine exemplary samples from the validation dataset. All patches were normalized individually for visualization purposes and prediction and ground truth patches were normalized identically for all samples.

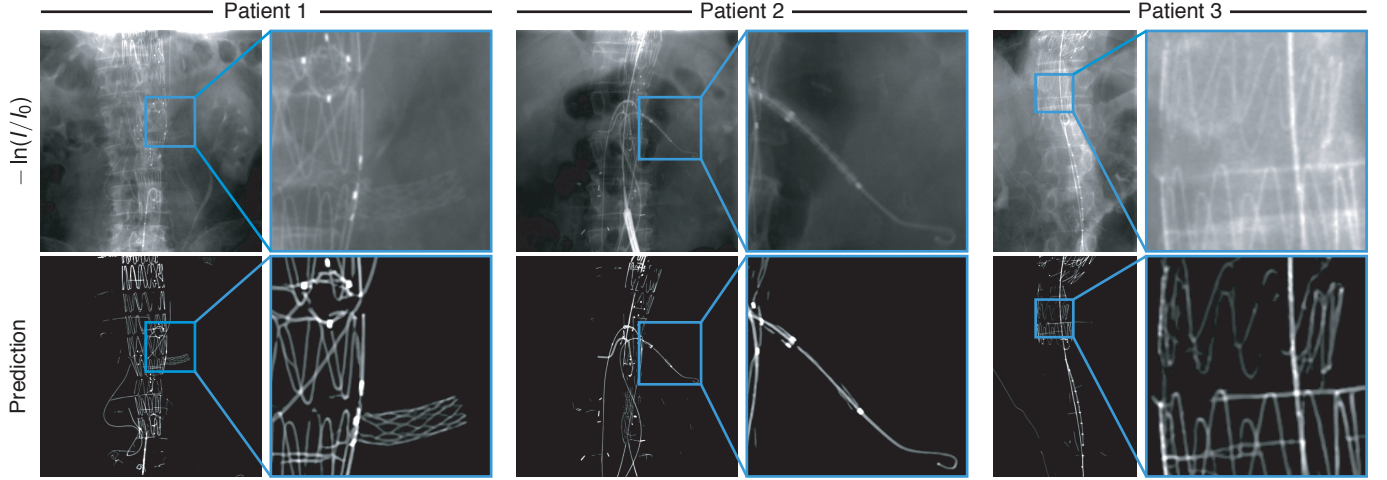


Fig. 5. Application of the deep tool extraction to three contrast-enhanced patient scans, which were acquired using a commercial C-arm system during a minimally invasive angioplasty with stenting. Image courtesy of Ziehm Imaging, Nürnberg, Germany.

and the respective network output $\text{DTR}(x; \rho)^{(n)}$,

$$\hat{\rho} = \arg \min_{\rho} \left[1 - \frac{2 \sum_{n,k} \text{DTR}(x; \rho)_k^{(n)} y_k^{(n)} + 1}{\sum_{n,k} \text{DTR}(x; \rho)_k^{(n)} + \sum_{n,k} y_k^{(n)} + 1} \right]. \quad (4)$$

To obtain a segmentation during inference, we threshold the probabilistic output of the network such that an output pixel value is rounded in order to yield the values 0 or 1, with 0 being a classification as background and 1 being a classification as an interventional tool.

F. Combined Pipeline

The combined pipeline is comprised of the following steps. First, four CBCT projections with an angular spacing of 45° are fed successively to the DTE, which extracts the tools from the patient anatomy. The volume is then sparsely reconstructed using the FDK reconstruction. The DTR network is applied to the sparse reconstruction by successively feeding chunks of consecutive slices to the network, leading to the segmentation of interventional tools present within the volume. This volume can be 3D rendered (e.g. using the software described in [24]) for visualization purposes.

III. RESULTS

A. Deep Tool Extraction

The deep tool extraction is trained and validated using simulated projection data as described in Sec. II-D. Figure 4 provides nine exemplary samples from the validation data together with the respective DTE prediction and ground truth. For all three interventional tools we observed little deviation from the ground truth. In some of the samples (blue arrows), three small structures can be noticed, which were detected by the network as being interventional material and do not belong to the simulated tools. A further investigation of the corresponding patient scan revealed that these structure are indeed surgical metal clips and were thus correctly detected by the network as interventional material. This is a strong indicator that the network generalized well, beyond those interventional tools seen during training.

The simulation involved in the training and validation of the deep tool extraction does not place the interventional tools in a physiological meaningful way inside the patient and furthermore neglects several physical effects such as scatter. To analyze the method's performance in a clinical setting, we therefore applied the deep tool extraction to three

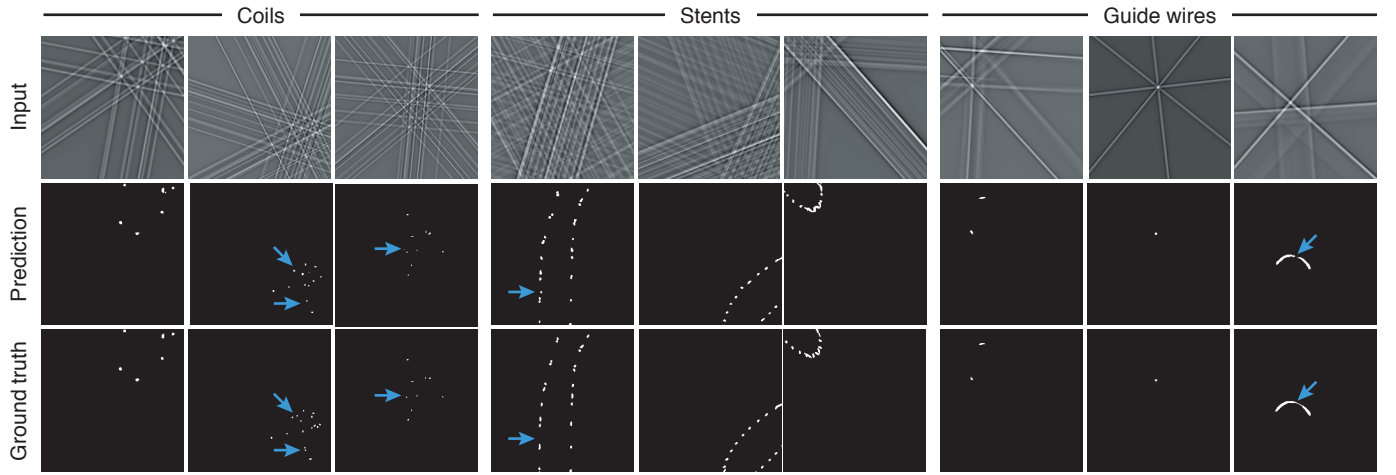


Fig. 6. Application of the deep tool reconstruction to nine exemplary samples from the validation dataset. All patches were normalized individually for visualization purposes and prediction and ground truth patches were normalized identically for all samples.

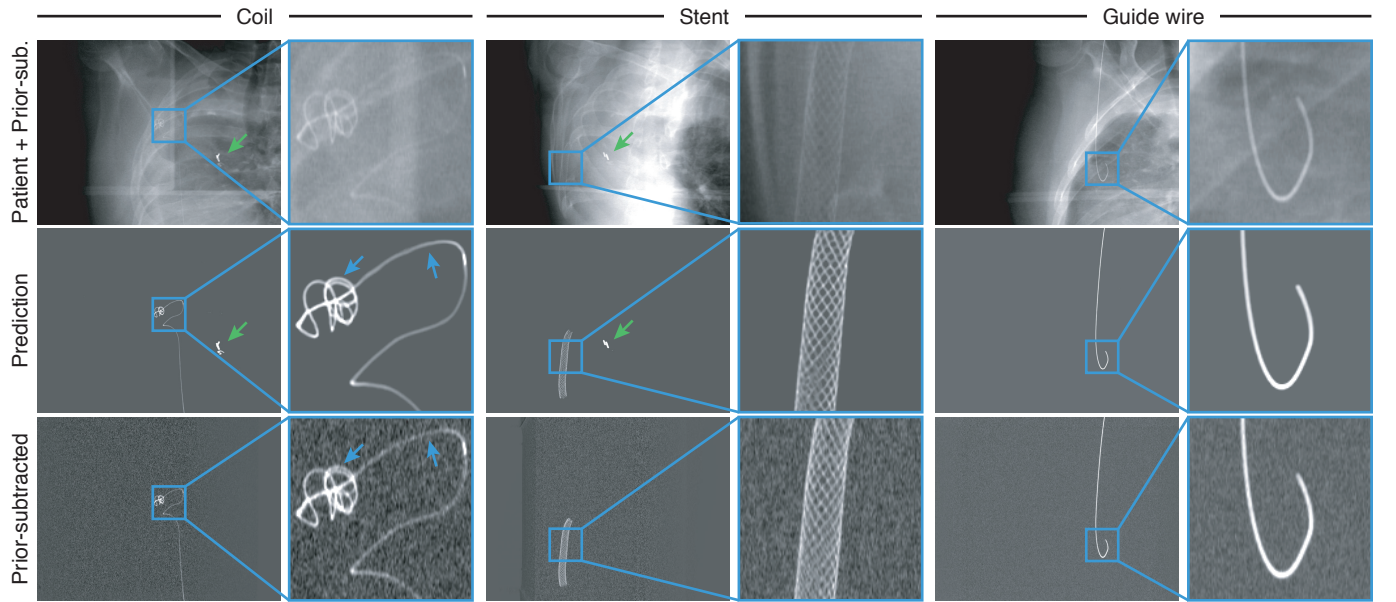


Fig. 7. Application of the deep tool extraction to phantom scans which were superimposed with a patient scan. Note that the noise distribution of the prior-subtracted scan is not corresponding to the projection values of the patient scan. The radiopaque markers (green arrows) are part of the patient scan and are therefore not visible in the prior-subtracted images.

fluoroscopy scans which were acquired using a commercial C-arm system (Ziehm Imaging, Nürnberg, Germany) during minimally invasive angioplasties with stenting (Fig. 5).

We notice significant deviation of the tools present in the patients from the tools which we had simulated as well as contrast media present in all three patients (clearly perceptible in Patient 3). Nonetheless, DTE detects most of the interventional tools present in the data, with only few exceptions such as few struts of some of the stents or the catheter in the second patient scan. The method's ability to detect radiopaque markers on the stents and guide wires is particularly remarkable, considering such markers were not included in the simulated data. Due to the lack of ground truth data for these scans, the analysis remains quantitatively.

B. Deep Tool Reconstruction

The deep tool reconstruction was trained to segment interventional tools in volumes which were sparsely reconstructed

TABLE II
DTR SEGMENTATION RESULTS EVALUATED USING DICE SCORE, PRECISION (POSITIVE PREDICTIVE VALUE) AND RECALL (SENSITIVITY) FOR DIFFERENT NUMBERS OF INPUT SLICES. HIGHLIGHTED ARE THE MAXIMUM VALUES FOR EACH METRIC ACROSS ALL CONFIGURATIONS.

C	z-coverage	Dice score	Precision	Recall
1	0.1 mm	0.751 ± 0.075	0.761 ± 0.056	0.745 ± 0.101
3	0.3 mm	0.781 ± 0.070	0.797 ± 0.047	0.769 ± 0.095
5	0.5 mm	0.794 ± 0.065	0.803 ± 0.047	0.790 ± 0.087
7	0.7 mm	0.794 ± 0.066	0.795 ± 0.044	0.797 ± 0.092
9	0.9 mm	0.796 ± 0.064	0.807 ± 0.050	0.788 ± 0.083
11	1.1 mm	0.794 ± 0.064	0.784 ± 0.046	0.807 ± 0.090
13	1.3 mm	0.796 ± 0.065	0.796 ± 0.046	0.800 ± 0.089
15	1.5 mm	0.799 ± 0.063	0.792 ± 0.045	0.809 ± 0.087
17	1.7 mm	0.797 ± 0.067	0.811 ± 0.045	0.787 ± 0.091

from only four x-ray projections. It is assumed that these projections contain only noise-free projection values of the interventional tools, which are perfectly extracted from the patient anatomy.

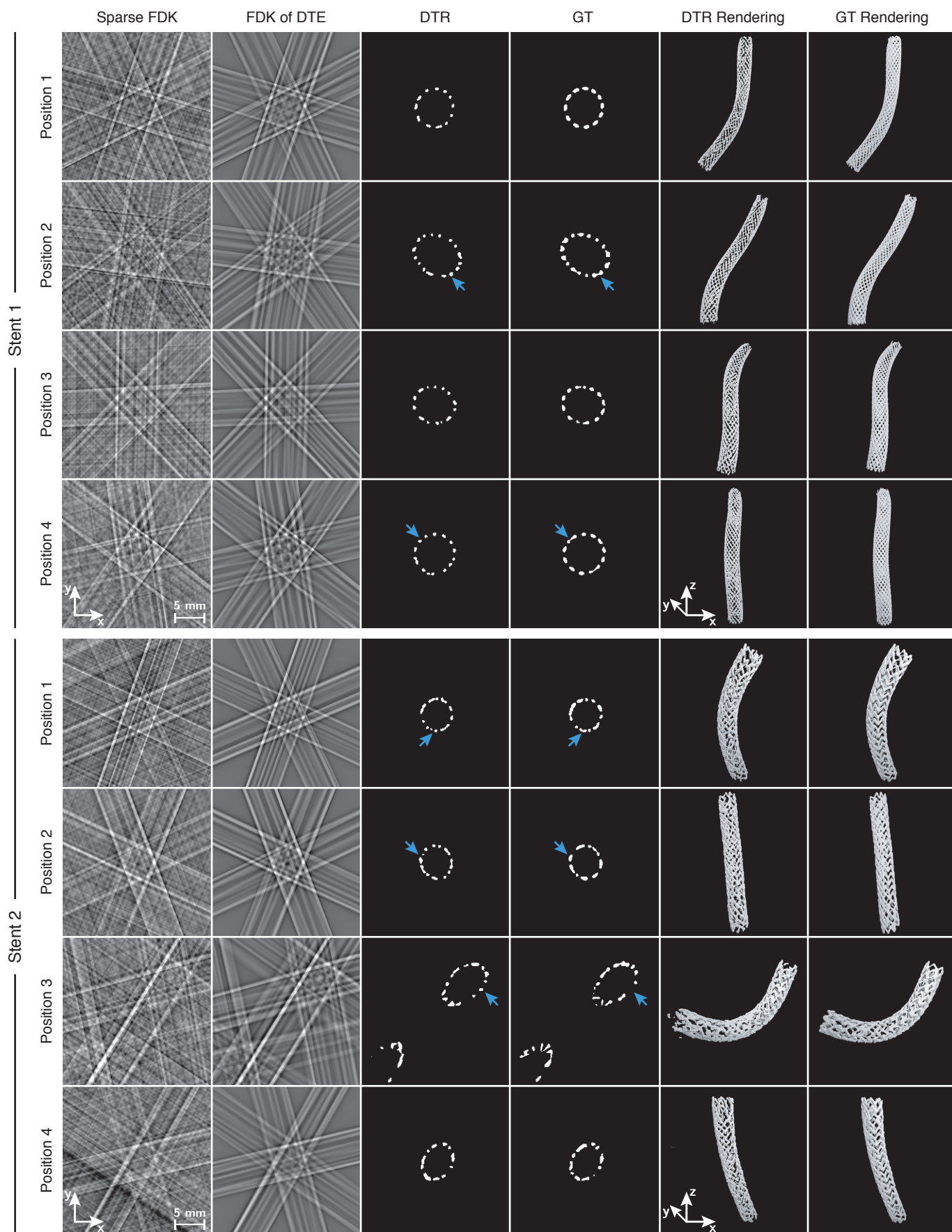


Fig. 8. Application of the combined pipeline to scans of the first test stent (top) and second test stent (bottom). The rows show different positions of the stents inside the vessel phantom, leading to different deformations. All slices are 224×224 pixels subsets. The renderings were scaled individually for improved visibility.

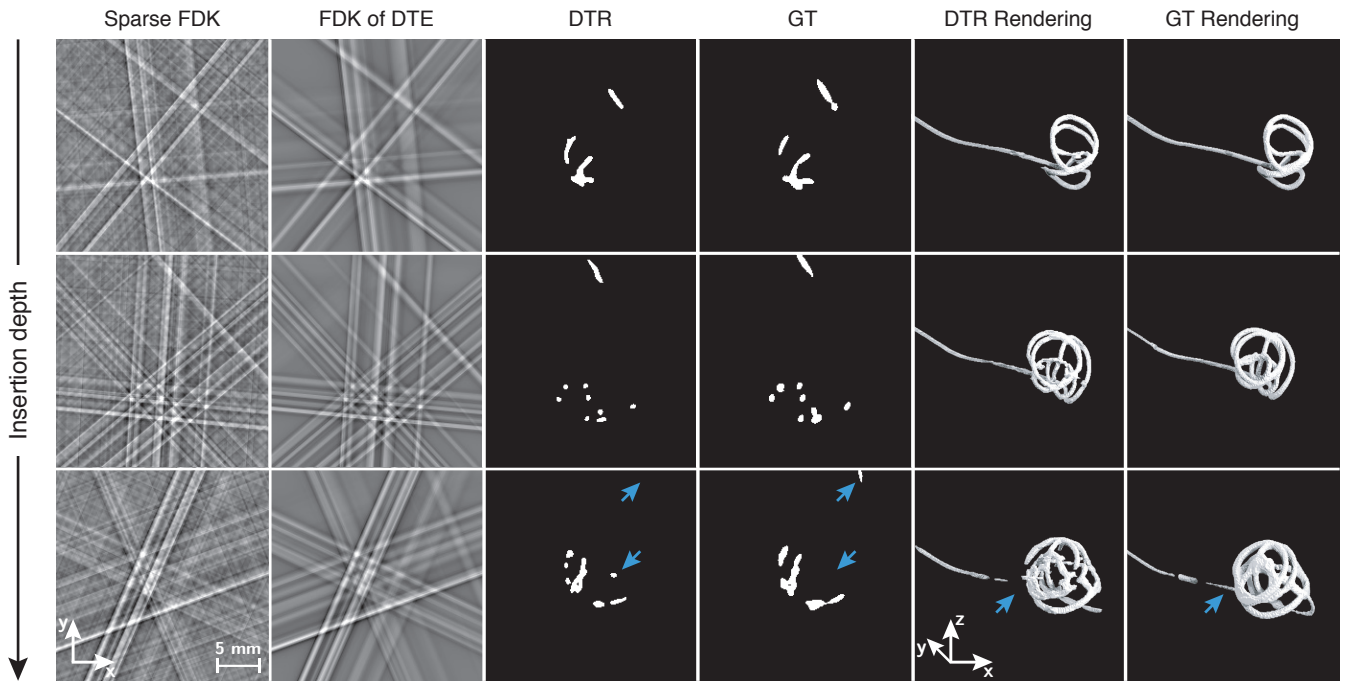


Fig. 9. Application of the combined pipeline to three scans of the coil at different insertion depths into the aneurysm. All slices are 224×224 pixels subsets.

We investigated the effect of the number of input slices C on the network's performance by evaluating the Sørensen–Dice coefficient (Dice score), precision, and recall on the validation dataset for different numbers of input slices (Table II). It can be concluded that the segmentation performance increases with an increasing number of input slices. This is expected due to the larger receptive field in z -direction associated therewith. However, this improvement is significant only for few slices, and we cannot observe a significant improvement for $C > 5 \pm 0.5$ mm.

In Fig. 6 we provide nine exemplary samples from the validation data together with the respective DTR segmentation and ground truth. For all samples shown, only little to no deviation from the ground truth was observed (blue arrows).

C. Combined Pipeline

Both submethods were combined and applied to measurements of commercially available interventional tools (Sec. II-C). Since these measurements were performed in phantoms, extracting the tools from the background is a trivial task, and consequently would lead to an overestimation of the performance of both DTE and DTR. Instead, the rawdata difference of interventional scan (phantom + tool) and prior (phantom only) was superimposed with a thorax patient scan, which was neither part of the training nor of the validation dataset for the deep tool extraction. The projection values of these projections were then normalized with the mean and standard deviation obtained during the training of the deep tool extraction prior to feeding them into the network.

Results of applying the deep tool extraction to scans of a stent, guide wire and coil are shown in Fig. 7. It was found that not only did DTE successfully extract the tools from the background, but it even enhanced the resolution of fine details such as the individual struts of the stent or parts of

TABLE III
MAPE OF DTE, EVALUATED ON DETECTOR PIXELS WHERE TOOLS ARE PRESENT IN THE PRIOR-SUBTRACTED SCAN.

Tool	MAPE [%]
Coils	13.2 ± 1.6
Stents	13.4 ± 2.1
Guide wires	6.0 ± 0.1

the coil (blue arrows). This can be explained by the deep tool extraction having been trained on simulated data, where the ground truth is noise-free and not degraded by blurring caused by the PSF of the system or by a misalignment between the interventional scan and the prior scan. Furthermore, DTE detected two radiopaque markers (green arrows) as interventional tools, even though radiopaque markers were never included in the training data. In Table III we report the mean absolute percentage error (MAPE) for the detector pixels, where a tool is present in the prior-subtracted scan. Note that, to reduce the influence of noise present in the prior-subtracted scan, we filtered both the DTE output and the prior-subtracted scan with a 3×3 pixels median filter.

Overall, little deviations from the prior-subtracted scan were observed, and some of these deviations may be explained by the prior-subtracted scan being degraded by noise. Together with the results seen in Fig. 5 this shows that the deep tool extraction generalized well beyond simulated data and can successfully extract interventional tools from background anatomy.

The combined pipeline was applied to scans of two stents (Fig. 8), the coil (Fig. 9) and two guide wires (Fig. 10). For the stents, scans of different positions inside the phantom, leading to various deformations of the stents are provided. For the coil three scans at different insertion depths into the aneurysm are shown.

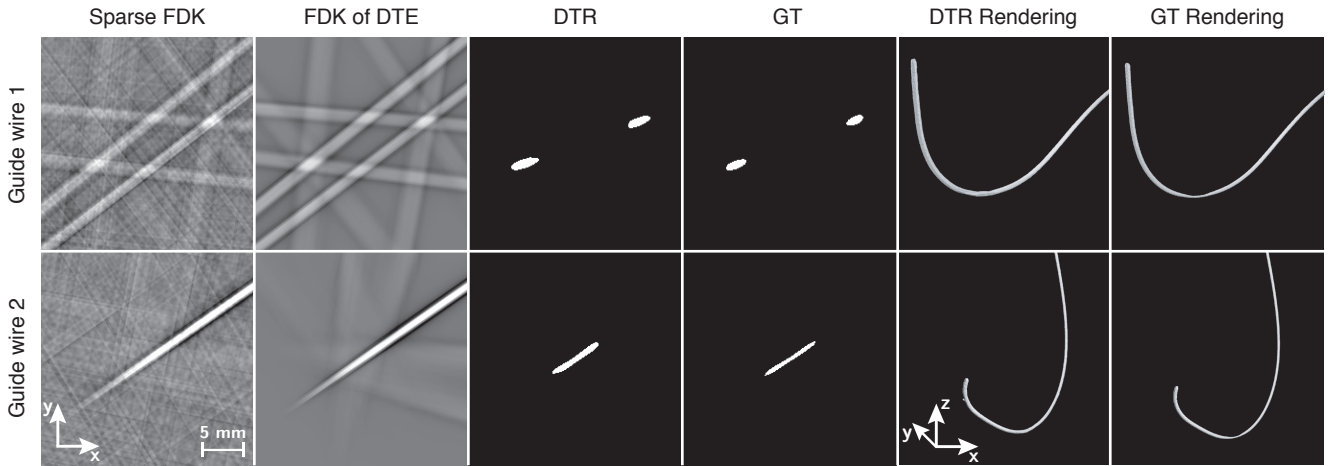


Fig. 10. Application of the combined pipeline to scans of two guide wires. All slices are 224×224 pixels subsets.

TABLE IV

SEGMENTATION RESULTS OF THE COMBINED PIPELINE APPLIED TO THE TEST DATA EVALUATED USING DICE SCORE, PRECISION AND RECALL.

Tool	Dice score	Precision	Recall
Coils	0.60 ± 0.02	0.74 ± 0.05	0.50 ± 0.04
Stents	0.58 ± 0.05	0.71 ± 0.06	0.49 ± 0.06
Guide wires	0.83 ± 0.05	0.79 ± 0.10	0.90 ± 0.07

A very good accordance with the ground truth was found for the stent reconstructions. This can be observed particularly well, when comparing the 3D renderings with each other. Most deviations were caused by split errors, where the DTR segmentation split one single intersection in the ground truth into two separate ones (see blue arrows). Furthermore, in the reconstruction of the second position of the second stent a slightly worse performance can be observed, most likely resulting from the stent being partially oriented in the x - y plane. In such cases a higher number of intersection points per plane occurs, making the reconstruction more ambiguous. The accuracy for such cases could be improved by increasing the number of projections, thereby reducing the number of possible solutions.

A similarly good performance as for the stent reconstructions can be observed for the coil reconstructions. For the scan where the coil is fully inserted into the aneurysm, however, we observe some deviations from the ground truth, specifically right after the coil leaves the micro catheter (blue arrows). A closer inspection of the DTE output revealed that some of these parts were not detected in one of the projections by the deep tool extraction and therefore could not be reconstructed by the deep tool reconstruction that followed.

For the guide wires, almost no deviations from the ground truth were found. This is expected due to their low number (usually less than four) of intersections with a given reconstructed slice. From discrete tomography it is well known that any slice with n intersections is uniquely determined by $m > n$ projections from mutually nonparallel directions [36]–[38], which is often the case for guide wires but usually not for coils or stents. We report the Dice score, precision and recall on the stents, guide wires and the coil in Table IV.

IV. DISCUSSION & OUTLOOK

The proposed pipeline is capable of reconstructing interventional tools without the need for a patient prior from only four CBCT x-ray projections. To our knowledge, this is the first time that CNNs were applied to realize tomographic interventional guidance and the results indicate that a deep learning-based tomographic interventional guidance could overcome the current drawbacks of conventional interventional guidance by providing the surgeon with full spatiotemporal information about the location and structure of interventional tools during a minimally invasive intervention. Not only could this enable the development of new procedures but it could also reduce the risk of complications for already existing procedures.

The complete pipeline has few limitations in its current state that we intend to investigate in future studies. A gantry with four rotating flat detectors and x-ray tubes is yet to be developed and it is unlikely that such a system will be produced in the near future due to the high associated costs. However, this work did not investigate the effect of reducing the number of projections further, potentially to two or three, where such a system would become feasible. Moreover, it may be possible to reconstruct the volumes with a temporal overlap, were the four projections are not acquired simultaneously. However, this would be possible only if the motion of the tools was either negligible or accounted for by the pipeline by incorporating motion correction. Moreover, we focused on a standard 2D U-net architecture and simple learning schemes for both DTE and DTR. Although some experiments involving attention-gated U-nets [39] were conducted, no significant advantage over a standard U-net was found. Nonetheless, more advanced network architectures and learning schemes are likely to improve the proposed method further. Particularly, leveraging the temporal information using a recurrent neural network based on long short-term memory [40]–[42] or gated recurrent units [43] and utilizing higher-level features using generative adversarial networks [44], [45] may be promising approaches for future studies. Another possible improvement could be made by jointly training the DTE and DTR networks end-to-end, thereby allowing the DTR network to account for possible errors made by the DTE.

REFERENCES

- [1] R. A. Kruger *et al.*, “Computerized fluoroscopy in real time for noninvasive visualization of the cardiovascular system,” *Radiology*, vol. 130, no. 1, pp. 49–57, 1979.
- [2] J. M. Tobis, O. Nalcioğlu, and W. L. Henry, “Digital subtraction angiography,” *Chest*, vol. 84, no. 1, pp. 68–75, 1983.
- [3] D. M. Pelz, A. J. Fox, and F. Vinuela, “Digital subtraction angiography: Current clinical applications,” *Stroke*, vol. 16, no. 3, pp. 528–536, 1985.
- [4] W. D. Jeans, “Computerized fluoroscopy in real time for noninvasive visualization of the cardiovascular system,” *The British Journal of Radiology*, vol. 63, no. 747, pp. 161–168, 1990.
- [5] D. Gervais and T. Sabharwal, *Interventional radiology procedures in biopsy and drainage*, ser. Techniques in Interventional Radiology. London, UK: Springer, 2010.
- [6] C. T. Dotter and M. P. Judkins, “Transluminal treatment of arteriosclerotic obstruction,” *Circulation*, vol. 30, no. 5, pp. 654–670, 1964.
- [7] A. Molyneux and R. Kerr, “International subarachnoid aneurysm trial (ISAT) of neurosurgical clipping versus endovascular coiling in 2143 patients with ruptured intracranial aneurysms: A randomized trial,” *Journal of Stroke and Cerebrovascular Diseases*, vol. 11, no. 6, pp. 304–314, 2002.
- [8] B. Jiang, M. Paff, G. P. Colby, A. L. Coon, and L.-M. Lin, “Cerebral aneurysm treatment: Modern neurovascular techniques,” *Stroke and vascular neurology*, vol. 1, no. 3, pp. 93–100, 2016.
- [9] R. F. Spetzler *et al.*, “The barrow ruptured aneurysm trial: 6-year results,” *Journal of Neurosurgery*, vol. 123, no. 3, pp. 609–617, 2015.
- [10] E. Bücheler, W. Hupe, E. U. Hertel, and H. Klosterhalfen, “Katheterembolisation von Nierentumoren,” *Fortschritte auf dem Gebiet der Röntgenstrahlen und der bildgebenden Verfahren*, vol. 124, no. 2, pp. 134–138, 2009.
- [11] R. J. T. Owen, “Embolization of musculoskeletal bone tumors,” *Seminars in Interventional Radiology*, vol. 27, no. 2, pp. 111–123, 2010.
- [12] A. Cowen, A. Davies, and M. Sivananthan, “The design and imaging characteristics of dynamic, solid-state, flat-panel x-ray image detectors for digital fluoroscopy and fluorography,” *Clinical Radiology*, vol. 63, no. 10, pp. 1073 – 1085, 2008.
- [13] M. F. Powell, D. DiNobile, and A. S. Reddy, “C-arm fluoroscopic cone beam CT for guidance of minimally invasive spine,” *Pain Physician*, vol. 13, no. 1, pp. 51–59, Jan. 2010.
- [14] R. Gupta, C. Walsh, I. S. Wang, M. Kachelrieß, J. Kuntz, and S. Bartling, “CT-guided interventions: Current practice and future directions,” in *Intraoperative Imaging and Image-Guided Therapy*. New York, NY: Springer, 2014, pp. 173–191.
- [15] Z. Neeman, S. A. Dromi, S. Sarin, and B. J. Wood, “CT fluoroscopy shielding: Decreases in scattered radiation for the patient and operator,” *Journal of Vascular and Interventional Radiology*, vol. 17, no. 12, pp. 1999–2004, 2006.
- [16] D. L. Donoho, “Compressed sensing,” *IEEE Transactions on Information Theory*, vol. 52, no. 4, pp. 1289–1306, 2006.
- [17] E. J. Candès, J. Romberg, and T. Tao, “Robust uncertainty principles: Exact signal reconstruction from highly incomplete frequency information,” *IEEE Transactions on Information Theory*, vol. 52, no. 2, pp. 489–509, 2006.
- [18] J. Kuntz, R. Gupta, S. Schönberg, W. Semmler, M. Kachelrieß, and S. Bartling, “Real-time x-ray-based 4D image guidance of minimally invasive interventions,” *European Radiology*, vol. 23, pp. 1669–1677, 2013.
- [19] J. Kuntz, B. Flach, R. Kueres, W. Semmler, M. Kachelrieß, and S. Bartling, “Constrained reconstruction for 4D intervention guidance,” *Physics in Medicine and Biology*, vol. 58, pp. 3283–3300, 2013.
- [20] L. Feldkamp, L. Davis, and J. Kress, “Practical cone-beam algorithm,” *Journal of the Optical Society of America*, vol. 1, no. 6, pp. 612–619, Jun. 1984.
- [21] B. Flach, M. Brehm, S. Sawall, and M. Kachelrieß, “Deformable 3D–2D registration for CT and its application to low dose tomographic fluoroscopy,” *Physics in Medicine and Biology*, vol. 59, pp. 7865–7887, 2014.
- [22] E. Eulig *et al.*, “Deep learning-aided CBCT image reconstruction of interventional material from four x-ray projections,” *Proceedings of the SPIE Medical Imaging Conference*, vol. 11312, pp. 378–384, Feb. 2020.
- [23] —, “Towards 4D interventional guidance: Reconstructing interventional tools from four x-ray projections using a deep neural network,” *Program of the 26th European Congress of Radiology (ECR)*, Mar. 2020.
- [24] Blender Foundation, “Blender: A 3D modelling and rendering package,” <http://www.blender.org>, 2018.
- [25] E. Eulig, J. Maier, M. Knaup, T. Koenig, K. Hörndler, and M. Kachelrieß, “Deep DSA (DDSA): Learning mask-free digital subtraction angiography for static and dynamic acquisitions protocols using a deep convolutional neural network,” *Program of the 25th European Congress of Radiology (ECR)*.
- [26] E. Eulig, J. Maier, M. Knaup, T. Koenig, K. Hörndler, and M. Kachelrieß, “Learned digital subtraction angiography (Deep DSA): Method and application to lower extremities,” *Proceedings of the 13th International Meeting on Fully 3D Image Reconstruction*, vol. 11072, p. 1107223.
- [27] B. P. Welford, “Note on a method for calculating corrected sums of squares and products,” *Technometrics*, vol. 4, no. 3, pp. 419–420, Aug. 1962.
- [28] D. E. Knuth, *The Art of Computer Programming*, 3rd ed. Addison Wesley Longman, 1997.
- [29] O. Ronneberger, P. Fischer, and T. Brox, “U-net: Convolutional networks for biomedical image segmentation,” *International Conference on Medical Image Computing and Computer-Assisted Intervention*, pp. 234–241, 2015.
- [30] S. Ioffe and C. Szegedy, “Batch normalization: Accelerating deep network training by reducing internal covariate shift,” *International Conference on Machine Learning*, vol. 32, pp. 448–456, Jul. 2015.
- [31] Y. Lecun, “Efficient Object Localization using Convolutional Networks,” *IEEE Conference on Computer Vision and Pattern Recognition*, 2015.
- [32] V. Nair and G. E. Hinton, “Rectified linear units improve restricted boltzmann machines,” *International Conference on Machine Learning*, vol. 10, pp. 807–814, Jun. 2010.
- [33] K. He, X. Zhang, S. Ren, and J. Sun, “Delving deep into rectifiers: Surpassing human-level performance on imagenet classification,” *IEEE International Conference on Computer Vision*, pp. 1026–1034, Dec. 2015.
- [34] A. Paszke *et al.*, “Pytorch: An imperative style, high-performance deep learning library,” in *Advances in Neural Information Processing Systems* 32, 2019, pp. 8026–8037.
- [35] D. P. Kingma and J. Ba, “Adam: A method for stochastic optimization,” *International Conference on Learning Representations*, vol. 3, 2015.
- [36] R. J. Gardner and P. Grizzmann, “Discrete tomography: Determination of finite sets by x-rays,” *Transactions of the American Mathematical Society*, vol. 349, no. 6, pp. 2271–2295, 1997.
- [37] A. Rényi, “On projections of probability distributions,” *Acta Mathematica Hungarica*, vol. 3, no. 3, pp. 131–142, 1952.
- [38] G. Bianchi and M. Longinetti, “Reconstructing plane sets from projections,” *Discrete & computational geometry*, vol. 5, no. 3, pp. 223–242, 1990.
- [39] O. Oktay *et al.*, “Attention U-net: Learning where to look for the pancreas,” *Medical Imaging with Deep Learning*, Jul. 2018.
- [40] S. Hochreiter and J. Schmidhuber, “Long short-term memory,” *Neural computation*, vol. 9, pp. 1735–1780, 1997.
- [41] F. A. Gers, J. A. Schmidhuber, and F. A. Cummins, “Learning to forget: Continual prediction with LSTM,” *International Conference on Artificial Neural Networks*, vol. 2, pp. 850–855, 1999.
- [42] —, “Learning to forget: Continual prediction with LSTM,” *Neural Computation*, vol. 12, no. 10.
- [43] K. Cho *et al.*, “Learning phrase representations using RNN encoder-decoder for statistical machine translation,” *Conference on Empirical Methods in Natural Language Processing*, pp. 1724–1734, 2014.
- [44] I. Goodfellow *et al.*, “Generative adversarial nets,” *International Conference on Neural Information Processing Systems*, vol. 2, pp. 2672–2680, 2014.
- [45] A. Radford, L. Metz, and S. Chintala, “Unsupervised representation learning with deep convolutional generative adversarial networks,” *arXiv preprint arXiv:1511.06434*, 2015.